#25-144
2025 AFS Proceedings ©American Foundry Society

Toward a More Complete Quantitative Model of Recarburizer Dissolution in Liquid Iron

Robert J. Umpleby
Miller and Company LLC, Rosemont, Illinois, U.S.A.

ABSTRACT

It is shown that the combination of the uniformly shrinking particle model with the classic diffusion layer model of dissolution can be used to predict the dissolution curve for a recarburizer. The method utilizes a transformation of the mass distribution of particle size into a number distribution, thereby allowing the initial interfacial surface area to be estimated. The shrinking particle model then permits the continuously changing surface area to be quantified for the duration of the dissolution process, enabling an analytical solution to the Hixson-Crowell equation. The applicability of the method is demonstrated for a hypothetical addition of graphite to a ductile iron melt. The results are consistent with published experimental data for graphite dissolution in molten iron. The practical implications of the model for recarburizer additions are discussed, including the effects of particle size, agitation, temperature, nature of the recarburizer, and production practices in the foundry.

Keywords: recarburizer, dissolution, graphite, carbon, iron, recovery, Hixson-Crowell

INTRODUCTION

Since the pioneering work of Fick[i] to model molecular diffusion and that of Noyes and Whitney[ii] to elucidate the process of dissolution, investigators have been advancing our qualitative and quantitative understanding of the dissolution of solids in liquids. An excellent review by Siepmann summarizes the history of the experimentation and basic equations.[iii] Regarding the dissolution of carbon in liquid iron, Dahlke and Knacke were the first to apply such foundational concepts to characterize the process.[iv] Now, almost seventy years later, a great deal more is understood about the factors that determine the rate at which any given carbon dissolves in iron. There remains, however, a need for a quantitative model that reliably predicts the dissolution time for a recarburizer. Such a model would allow ferrous foundries to better understand the extent to which the properties of both the recarburizer and the iron affect dissolution time. This, in turn, would enable each foundry to select the best recarburizer for its operation and to make more accurate predictions of recarburizer recovery.

Many investigators of the carbon/molten iron system have used dissolution data to calculate the apparent overall dissolution coefficient (K), mass transfer coefficient (k_m), dissociation coefficient (k_d), and activation energy (E_a) for a variety of carbons.[1,v,vi,vii,viii,ix,x,xi,xii,xiii,xiv,xv,xvi,xvii,xviii,xix] The converse—predicting the time required for the dissolution of a given carbon—presents a different challenge. Even in the case where the rate coefficient is known or can be estimated, there is still the effect of the continually changing surface area of the carbon to consider. Presented here is a method for explicitly accounting for the variable surface area throughout the dissolution process. This, in turn, allows the direct calculation of the carbon concentration as a function of time using an analytical solution to the Hixson-Crowell equation.

THEORY

DIFFUSION LAYER MODEL OF DISSOLUTION

The process of dissolution of a carbon particle in molten iron has been described by many investigators as consisting of two steps (Figure 1).[12,15,17,19,xx] In the first step, individual carbon atoms dissociate from the carbon particle to the boundary layer, where they associate with the molten iron.[xxi] In the second step, the individual atoms of carbon diffuse across the boundary layer to the bulk iron. The driving force of this process is the concentration gradient between the particle surface and the bulk iron. The concentration of carbon in the boundary layer is highest near the surface of the particle, decreasing with distance from the particle. The dissolution process for any given carbon atom is complete when it passes from the

boundary layer to the bulk iron, where the concentration of carbon atoms is uniform. Taken together, the dissociation and diffusion steps constitute the diffusion layer model, which has been applied to many solute/solvent systems.[3]

The quantitative modeling of the dissolution process depicted in Figure 1 is well-established.[3,15,19,20] The rate of dissociation of carbon atoms from a carbon particle is given in Eqn. 1, where C_s (wt. %) is the solubility of carbon, C_i (wt. %) is the concentration of carbon atoms at the interface between the carbon particle and the iron, k_d (m s^{-1}) is the dissociation coefficient, S (m^2) is the surface area of the interface between the carbon particle and the iron, V (m^3) is the total volume of the iron melt, and t (s) is the time. Similarly, the rate of diffusion of the dissociated carbon atoms across the boundary layer to the bulk iron is given in Eqn. 2, where C (wt. %) is the concentration of carbon atoms in the bulk iron at time t and k_m (m s^{-1}) is the mass transfer coefficient. Equations 1 and 2 assume that the recarburizer surface at the interface with the iron is wetted, and that the temperature and agitation are constant.

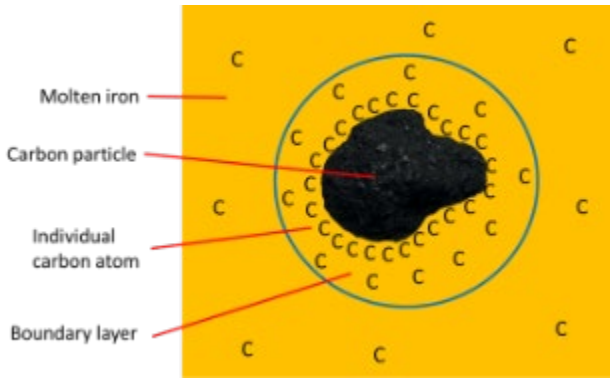

Figure 1. The diffusion layer model consists of the dissociation of individual carbon atoms from the particle and subsequent diffusion of those atoms across the boundary layer to the bulk iron. The driving force of the dissolution process is the carbon concentration gradient through the thickness of the diffusion layer.

$$\frac{dC_i}{dt} = \frac{k_d S}{V}(C_s - C_i) \qquad \textbf{Eqn. 1}$$

$$\frac{dC}{dt} = \frac{k_m S}{V}(C_i - C) \qquad \textbf{Eqn. 2}$$

There are two special cases in which Eqn. 4 can be simplified. If the rate of diffusion is much slower than the dissociation rate ($kd >> km$), then $kd + km \approx kd$ and $k \approx km$. This is known to be the case, for example, for the dissolution of high-purity graphite in molten iron.[6,12,16,17] Conversely, if dissociation is much slower than diffusion ($km >> kd$), then $kd + km \approx km$ and $k \approx kd$.

CONSTANT INTERFACIAL SURFACE AREA

Equation 3 is a variation of the Nernst-Brunner expression.[3] Mathematically, this differential equation presents a classical initial value problem. The equation can be solved analytically by integration to yield $C(t)$, the concentration of carbon dissolved in the iron at time t. The functional form of $C(t)$ depends on the assumption for S. If S is effectively constant for the reaction time under consideration, then the apparent dissolution coefficient is $K = kS/V$ and the well-known Noyes-Whitney equation results (Eqn. 5).[3] Equation 5 can be rearranged to give Eqn. 6. If C_0 is the initial concentration of dissolved carbon, then $C = C_0$ at $t = 0$ and the solution to Eqn. 6 is Eqn. 7. If K is unknown, it can be determined from dissolution data by rearranging Eqn. 7 into a linear form (Eqn. 8), where the slope of $\ln(C_s - C)$ *vs.* t is $-K$. This method has been employed by investigators to determine the value of K,[5,6,7,8] which can be assumed to be constant during the initial phase of dissolution (since there is little change in the interfacial surface area). This has allowed researchers to probe the dependence of dissolution rate on such variables as recarburizer structure and composition, iron composition, temperature, and agitation rates.[5-19]

$$\frac{dC}{dt} = K(C_s - C) \qquad \textbf{Eqn. 5}$$

$$\int \frac{1}{C_s - C} dC = \int K dt \qquad \textbf{Eqn. 6}$$

$$C(t) = C_s - (C_s - C_0)e^{-Kt} \qquad \textbf{Eqn. 7}$$

$$\ln(C_s - C) = \ln(C_s - C_0) - Kt \qquad \textbf{Eqn. 8}$$

VARIABLE INTERFACIAL SURFACE AREA

Predicting the entire dissolution curve, $C(t)$, for a recarburizer presents a more difficult challenge. Even if the dissolution coefficient k is known, solving Eqn. 3 requires knowledge of S. The interfacial surface area changes continuously from the moment the first recarburizer particles are wetted by the iron until the saturation point has been reached or until all the particles have dissolved. Complicating the problem further is that a recarburizer is normally characterized by a relatively broad distribution of particle sizes, shapes, and internal pores that may or may not be accessible to the iron. A

complete quantitative model of the surface area that is accessible to the iron would take these factors into consideration.

Hixson and Crowell solved Eqn. 3 for the general case of a single, convex crystal of ordinary shape whose surface area varies continuously over time. [12,15, 17, 19, 20] Their approach begins by converting Eqn. 3 to its mass form using Eqns. 9-11, where m is the mass of undissolved carbon at time t, m_s is the mass of carbon required to saturate the iron, m_1 is the initial mass of dissolved carbon (the mass at $t = 0$), and m_0 is the mass of the carbon addition. Combining Eqns. 9-11 with Eqn. 3 yields Eqn. 12.

$$dC = -\frac{dm}{V} \qquad \textbf{Eqn. 9}$$

$$C_s = \frac{m_s}{V} \qquad \textbf{Eqn. 10}$$

$$C = \frac{m_1 + m_0 - m}{V} \qquad \textbf{Eqn. 11}$$

$$\frac{dm}{dt} = -\frac{kS}{V}(m_s - m_1 - m_0 + m) \qquad \textbf{Eqn. 12}$$

A key insight of Hixson and Crowell is that Eqn. 12 can be solved analytically for a crystal of varying surface area if S is expressed as a function of m. The procedure is then analogous to that employed to solve Eqn. 3.

Rearrangement of Eqn. 12 leads to Eqn. 13. In the case of a single crystal, the well-known relation for ordinary convex shapes that S varies as $V^{2/3}$ can be applied. The result is Eqn. 14, where k_s is a shape factor ($k_s = 4.84$ for a sphere) and V_c, m, and ρ are the crystal volume, mass, and density, respectively. Combining Eqns. 13 and 14 yields Eqn. 15, where $k' = kk_s'$. Equation 16 is the solution, where $g = m_s - m_1 - m_0$, $a = g^{1/3}$, $b = m_0^{1/3}$, and $x = m^{1/3}$. The function $m(t)$ is generated for any given value of k by substituting m values into Eqn. 16 over the range of $m_1 \leq m \leq m_1 + m_0$ (subject to $m_1 + m_0 \leq m_s$) which yields the corresponding t values for the entire dissolution curve. Certain special cases allow the use of simpler expressions in place of Eqn. 16.[22]

$$\int \frac{1}{S(m)(m_s - m_1 - m_0 + m)}\,dm = \int -\frac{k}{V}\,dt \qquad \textbf{Eqn. 13}$$

$$S = k_s V_c^{2/3} = k_s \frac{m^{2/3}}{\rho^{2/3}} = k_s' m^{2/3} \qquad \textbf{Eqn. 14}$$

$$\int \frac{1}{m^{2/3}(m_s - m_1 - m_0 + m)}\,dm = \int -\frac{k'}{V}\,dt \qquad \textbf{Eqn. 15}$$

$$\frac{V}{a^2}\left[\sqrt{3}\tan^{-1}\frac{2\sqrt{3}a(b-x)}{3a^2+(2b-a)(2x-a)} + 1.1513\log\frac{(a+b)^2(a^2-ax+x^2)}{(a+x)^2(a^2-ab+b^2)}\right] = k't \qquad \textbf{Eqn. 16}$$

Equations 15 and 16 are adequate for a single crystal. They work equally well in the case of multiple particles of ordinary, convex shape (for example, spherical or prismatic) if the particle population is monodisperse and if the dissociation of a particle takes place only at its external surface (that is, if any internal porosity is inaccessible to the solvent). This is because the total interfacial surface area in this instance is the product of the external surface area of a single particle and the number of particles, both of which are readily calculated for a given mass of particles if the particle density and radius are known. However, different expressions are required in the case of a broader particle distribution and/or a particle containing pores which can be penetrated by the solvent. While typical recarburizers are clearly polydisperse, the accessibility of pores to the iron during dissolution is less obvious. The theoretical treatment continues under the assumption that only the external surface of a carbon particle can interface with the iron. The relaxation of this assumption is discussed later. Finding an expression for S in the case of a polydisperse recarburizer begins with an estimate of the initial surface area. This can be calculated from an ordinary mass distribution of particle size (typically available from the recarburizer supplier) under the simplifying assumption of spherical particles. Let $f_m(r)$ be the initial unnormalized mass distribution of the particle radius, where r is the radius of a carbon particle at the midpoint between sieve sizes. [24] The total mass of the recarburizer, $F_m(r)$, is the unnormalized cumulative mass distribution given in Eqn. 17, where m_i is the mass of the particles having radius r_i.[25]

$$F_m(r) = m_0 = \sum_{i=1}^{n} m_i \qquad \textbf{Eqn. 17}$$

The surface area, volume, and mass of a particle with radius r_i are given in Eqns. 18-20. The particle density, ρ, in Eqn. 20 can be measured or estimated via literature values. Thus, the number of particles with radius r_i can be calculated via Eqn. 21. Let $f_N(r)$ and $F_N(r)$ be the initial unnormalized number distribution of the particle radius and cumulative number distribution, respectively. Then the total number of particles added to the furnace is given in Eqn. 22, and Eqn. 23 gives their total surface area.

$$S_{part_i} = 4\pi r_i^2 \quad \textbf{Eqn. 18}$$

$$V_{part_i} = \frac{4\pi r_i^3}{3} \quad \textbf{Eqn. 19}$$

$$m_{part_i} = V_{part_i}\rho \quad \textbf{Eqn. 20}$$

$$N_i = \frac{m_i}{m_{part_i}} \quad \textbf{Eqn. 21}$$

$$F_N(r) = N_0 = \sum_{i=1}^{n} N_i \quad \textbf{Eqn. 22}$$

$$S_0 = \sum_{i=1}^{n} S_i = \sum_{i=1}^{n} N_i S_{part_i} \quad \textbf{Eqn. 23}$$

As the recarburizer dissolves, its total surface area decreases. Bullard et al. have shown that the uniformly shrinking particle model can be used to calculate the change in the surface area of a polydisperse particle population as dissolution progresses. [26] Assuming that the dissolution flux is independent of particle size, the radii of all particles shrink at the same rate (Figure 2). [27] This is readily apparent in Eqn. 24. Let the dissolution flux J (kg m^2 s^{-1}) be the instantaneous change in the mass of the undissolved recarburizer per unit area per second. Recognizing that $dm = \rho dV = \rho S dr$, it is clear that dr/dt is independent of the radius and is, in fact, equal to the dissolution flux at time t divided by the particle density (assumed to be constant for all particles).

$$J = \frac{dm}{Sdt} = \frac{\rho dV}{Sdt} = \frac{\rho Sdr}{Sdt} = \frac{\rho dr}{dt} \Rightarrow \frac{dr}{dt} = \frac{J}{\rho} \quad \textbf{Eqn. 24}$$

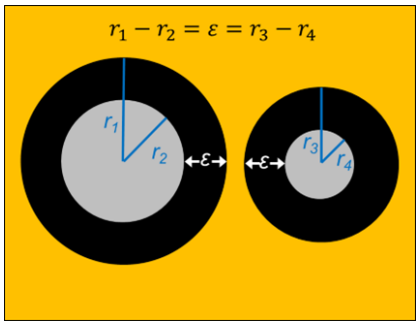

Figure 2. According to the uniformly shrinking particle model, the radii of all particles shrink at the same rate at any given time, t. Thus, the change in the radius, Δr = ε, is the same for all particles after Δt = t_1 - t_2.

Let ε be the decrease in particle radius after a given time t. The particles with radius $r \leq \varepsilon$ dissolve completely, in which case those particles are no longer included in the distribution. The new radius for each remaining particle category is $r - \varepsilon$. Assuming no particle breakup, the number of particles within each of the remaining mass fractions m_i is unchanged (only the radius r_i has changed). This leads to the conditional unnormalized number distribution of the particle radius $g_N(r|\varepsilon)$ and the cumulative distribution $G_N(r|\varepsilon)$. The cumulative distribution is given in Eqn. 25. If the original radii of all particles are greater than ε, then the total number of particles is unchanged and $N = N_0$. If there are particles whose original radius is less than or equal to ε, then those particles dissolve completely and $N < N_0$. In both cases, the total mass of undissolved carbon m and total surface area S has decreased. Their new values can be calculated in much the same way as their original values were determined. Substituting the new radius $r - \varepsilon$ into Eqns. 18-20 gives the new surface area, volume, and mass of a particle for each fraction of particles. Substituting N_i and the new particle mass $m_{part,i}$ into Eqn. 21 gives the new m_i for each mass fraction, the sum of which is the new total mass of undissolved recarburizer m at time t. The new total surface area S at time t is given in Eqn. 23 if S_0 is replaced by S. Thus, the function $S(m)$ is generated by choosing various ε values in the range $0 \leq \varepsilon \leq r_{max}$. Each value of ε yields corresponding values of m and S. Fitting this data with a suitable function gives $S(m)$. Substituting this expression for $S(m)$ in Eqn. 13 and integrating yields the solution.

$$G_N(r|\varepsilon) = N = \sum_{i=1}^{n} N_i \quad \textbf{Eqn. 25}$$

APPLICATION TO A HYPOTHETICAL CARBON ADDITION FOR A DUCTILE IRON

Here the application of the diffusion layer model combined with the uniformly shrinking particle model is demonstrated for a hypothetical carbon addition to an iron melt. Specifically, the model is applied to a 1% addition of polydisperse graphite (Graphite 1) during the process of making a ductile iron. The assumed initial properties of the iron and recarburizer are provided in Tables 1 and 2, respectively. Such data would normally be available to the foundry.

Table 1. Initial Iron Properties

Mass (kg)	1.0 x 10^4
Density (kg m^{-3})	7.0 x 10^3
Volume (m^3)	1.4
Temperature	2700F (1480C)
Carbon (wt. %)	2.50
Silicon (wt. %)	1.60
Phosphorus (wt. %)	0.010
Sulfur (wt. %)	0.015
Manganese (wt. %)	0.200

Table 2. Properties of Graphite 1

Mass (kg)	100.
Particle density (kg m^{-3})	1.5 x 10^3
Fixed carbon (wt. %)	98.95
Ash (wt. %)	0.50
Volatiles (wt. %)	0.50
Moisture (wt. %)	0.05
Sulfur (wt. %)	0.05

The objective is to solve Eqn. 13 for the graphite addition, enabling the generation of $m(t)$ and its corresponding concentration form, $C(t)$. Beginning with the values that can be substituted immediately into Eqn. 13, Tables 1 and 2 indicate that $V = 1.4$ m^3, $m_1 = 250.$ kg, and $m_0 = 100.$ kg. The value of m_s can be determined by experiment or calculated from an estimate of C_s using Eqn. 26, where T is the temperature in Celsius and Si, P, S, and Mn are the concentrations by weight of silicon, phosphorus, sulfur, and manganese, respectively.[1] According to Eqn. 26, C_s = 4.61 wt. %. Multiplying by the final total mass of 10,100 kg yields m_s = 465 kg.

$$C_S = 1.30 + 0.00257T - 0.31Si - 0.33P - 0.40S + 0.027Mn \qquad \textbf{Eqn. 26}$$

The initial surface area is derived from the initial mass distribution of the particle diameter (normally available from the supplier of the recarburizer and easily verified using standard testing sieves). A realistic example for a graphitized petroleum coke (with nominal sizing of 6.4 x 0.2 mm, or ¼" x 70M) is shown in Figure 3. Assume spherical particles and that the midpoint of the diameter range for each particle fraction is the representative diameter for all the particles in that fraction. The result is shown graphically in Figure 4, where diameter has been converted to radius. Applying Eqns. 18-21 to each of the seven particle fractions in Figure 4 yields the number distribution of the particle radius (Figure 5). Finally, Eqn. 23 is applied to give the surface area for each of the seven number fractions (Figure 6) and, by summation, the total initial surface area S_0. Tables 3 and 4 show the initial mass distribution and calculated data, respectively, for each of the seven fractions that comprise the graphite addition to the iron.

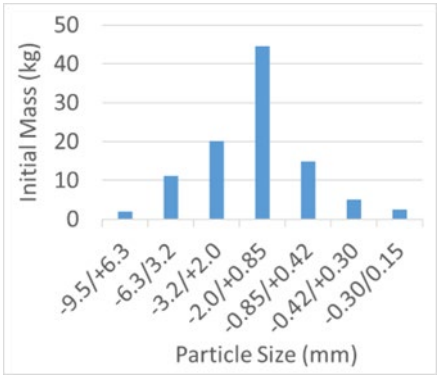

Figure 3. The initial mass distribution of the particle size for Graphite 1 consists of seven particle fractions.

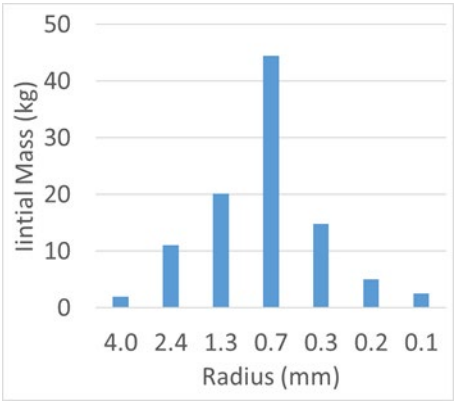

Figure 4. Assuming spherical particles and taking the midpoint of each particle fraction in Figure 3 to be the diameter yields a discrete mass distribution of the particle radius.

As described above, the undissolved mass and corresponding surface area of the graphite over time are determined by letting the decrease in particle radius ε vary over the range $0 \le \varepsilon \le r_{max}$. An example is shown in Table 5 for $\varepsilon = 0.050$ mm. Applying Eqns. 18-21 and 23 (where S is substituted for S_0) yields the new values of the undissolved mass (m_i) and surface area (S_i) for each particle fraction. The summation of these values gives the new total undissolved mass (m) and surface area (S). This procedure is repeated with various ε values to cover the entire range of the initial particle radii. When $r_i - \varepsilon < 0$ for a given fraction of particles, it indicates that the fraction of particles is completely dissolved and $N_i = 0$ for that fraction. Table 6 shows the results of these calculations for various values of ε. A plot of S *vs.* m is shown in Figure 7. In this example, a quadratic function provides a close empirical fit to the data. [29] Substituting this function for $S(m)$ in Eqn. 13 yields Eqn. 27. Subsequent integration gives the solution (Eqn. 28), where $h = m_1 + m_0 - m_s$ (for

simplicity). The derivation of Eqn. 28 is provided in the Appendix.

$$\int \frac{1}{(am^2+bm)(m_s-m_1-m_0+m)}dm = \int -\frac{k}{V}dt \qquad \textbf{Eqn. 27}$$

Table 3. Initial Mass Distribution of Graphite 1

Fraction (mm)	m_i (kg)	D_i (mm)*	r_i (mm)
-9.52/+6.35	2.0	7.94	3.97
-6.35/+3.35	11.1	4.85	2.42
-3.35/+2.00	20.2	2.68	1.34
-2.00/+0.850	44.4	1.42	0.713
-0.850/+0.425	14.8	0.638	0.319
-0.425/+0.300	5.06	0.363	0.181
-0.300/+0.150	2.50	0.256	0.128
All fractions	100.0		

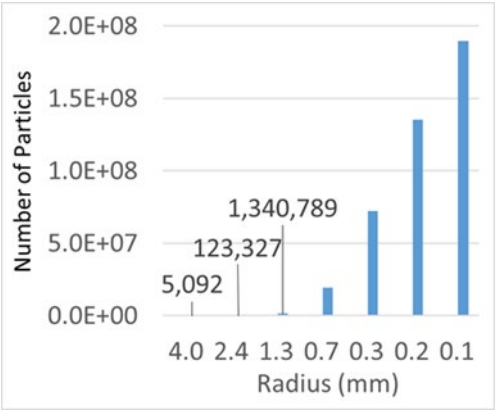

Figure 5. The initial number distribution of the particle radius is derived using Eqns. 18-21.

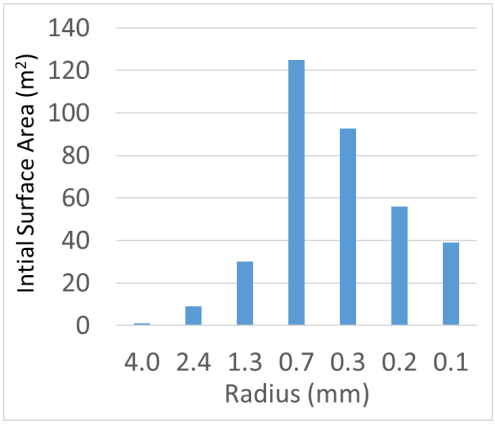

Figure 6. Using Eqn. 23, the initial surface area distribution of the particle radius is generated from the number distribution in Figure 5.

Table 4. Calculated Data for Initial Particle Fractions for Graphite 1

r_i (mm)	S_{part} (x 10^6 m^2)	V_{part} (x 10^{10} m^3)	m_{part} (x 10^6 kg)	N_i (x 10^{-4})	S_i (m^2)
3.97	198.	2620	393	0.509	1.01
2.42	73.9	59.7	89.6	12.3	9.11
1.34	22.5	100.	15.0	134	30.1
0.713	6.38	15.2	2.27	1960	125
0.319	1.28	1.36	0.203	7250	92.6
0.181	0.413	0.249	0.0374	13,500	55.8
0.128	0.206	0.0878	0.0132	19,000	39.1
All particles				41,800	352

Table 5. Calculated Values of m_i and S_i for Graphite 1 with ε = 0.050 mm

Initial r_i (mm)	$r_i - \varepsilon$ (mm)	N_i (x 10^{-4})	m_i (kg)	S_i (m^2)
3.97	3.92	0.509	1.93	0.983
2.42	2.37	12.3	10.4	8.74
1.34	1.29	134	18.0	27.9
0.713	0.663	1960	35.7	108
0.319	0.269	7250	8.84	65.8
0.181	0.131	13,500	1.92	29.3
0.128	0.078	19,000	0.566	14.5
All particles		41,800	77.3	255

Table 6. Total Undissolved Mass and Surface Area of Graphite 1 for Various Values of ε

ε (mm)	*m* (kg)	*S* (m²)
0.00	100.0	352
0.05	77.3	255
0.10	61.0	182
0.15	49.1	138
0.20	39.9	108
0.30	27.1	68.1
0.40	18.6	46.0

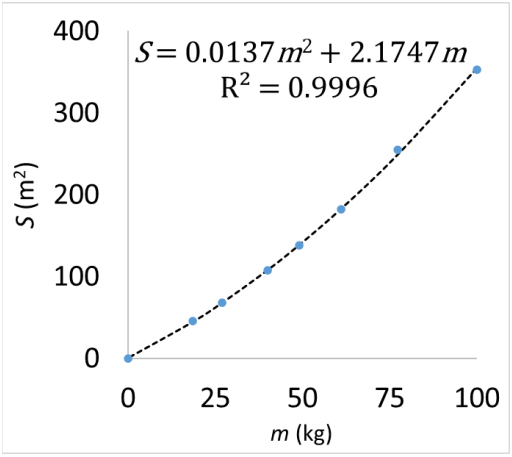

Figure 7. An empirical fit to the data in Table 6 yields S as a function of m for Graphite 1.

Using Eqn. 28 to generate $m(t)$ requires knowledge (or an estimate) of the dissociation coefficient k. Its value depends primarily on the molecular structure and composition of the recarburizer, temperature, and agitation. Many of the values of k found in the recarburizer literature are in the range of 10^{-5}-10^{-4} m s^{-1}.[1] **Error! Bookmark not defined.,Error! Bookmark not defined.,Error! Bookmark not defined.,Error! Bookmark not defined.,Error! Bookmark not defined.,Error! Bookmark not defined.**

Highly graphitic recarburizers in well-agitated melts tend to be associated with the higher part of this k range. In practice, a foundry's historical recarburizer recovery data may be helpful for estimating k for a given recarburizer and set of furnace conditions. Such mass and time data can be entered into Eqn. 28 to yield the value of k. A k value of 10^{-4} m s^{-1} is assumed in the present example. The effect of k on dissolution time is discussed in the next section.

Substituting m values in the range of $0 < m \leq m_0$ into Eqn. 28 yields the corresponding values of t (Figure 8).[1] The equivalent concentration curve (Figure 9) is generated with Eqn. 29, where m_{Fe} is the mass of the iron melt before the graphite addition. The dissolution is rapid, as the carbon recovery is greater than 90% within two minutes. This is to be expected, given the assumptions that all of the graphite is wetted at $t = 0$ as well as the relatively high dissolution coefficient ($k = 10^{-4}$ m s^{-1}). Loper and coworkers observed that a 0.5 wt. % addition of high-purity graphite at a similar temperature and starting carbon concentration took approximately five minutes to dissolve completely.[2] A summary of the dissolution data reported in the literature for graphite in molten iron is provided in Table 7. The results of this study are in good agreement with the published data, especially when the wide variety of experimental conditions represented in Table 7 is considered.

$$\frac{ah\ln(am_0+b)+b\ln(m_s-m_1)-(ah+b)\ln m_0}{bh(ah+b)} - \frac{ah\ln(am+b)+b\ln(m-h)-(ah+b)\ln m}{bh(ah+b)} = \frac{k}{V}t \qquad \textbf{Eqn. 28}$$

Table 7. Reported Dissolution Data for Graphite in Molten Iron

T	*K* (x 10³ s⁻¹)	*k* (x 10⁴ m s⁻¹)	E_a (kJ mol⁻¹)	t_{90} (min)*	Ref.
2367-2818F (1297-1548C)		0.27-3.0			13
2552F (1400C)		0.9-4.2			14
2372-2912F (1300-1600C)		0.087-3.38	38.2-40.0		16
2642-2822F (1450-1550C)	16.68-20.74		54	5-10	7
2822F (1550C)		2.5	19.2	4-5	12
2705F (1485C)				4-8	30
2700F (1482C)				18	27
2696F (1480C)	2.5-25	0.10-1.0		1.6-16	This work

**Time required to dissolve 90% of the total possible carbon addition, calculated as $C = C_0 + 0.90(C_s - C_0)$.*

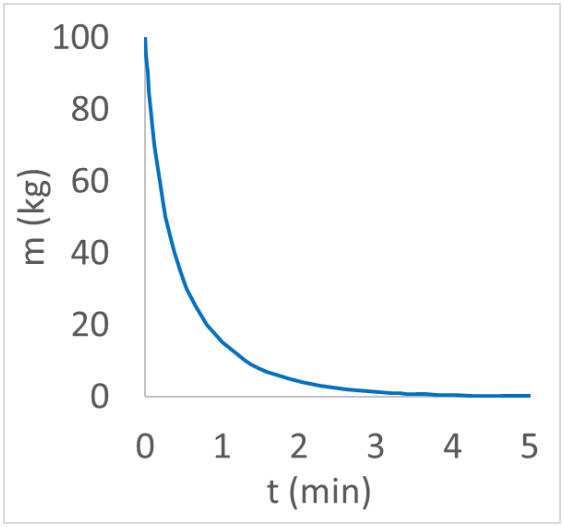

Figure 8. Equation 28 is utilized to generate m(t) for Graphite 1 (T = 2696F (1480C), k = 10^{-4}m s^{-1}).

The *K*-values in Table 7 for this work were calculated for the *k*-range 10^{-5}-10^{-4} m s^{-1} according to $K = kS/V$, where S = 352 m^2 at $t = 0$ (Table 4) and V =1.4 m^3 (Table 1).

The error bars in Fig. 9 were generated via a sensitivity analysis in which the values that would normally be measured or calculated from measured data (T, V, k, m_s, m_1, m_0, m_{Fe}, and the masses of the other components of the melt) were varied by 2%. This resulted in a maximum relative uncertainty in the value of t of approximately 20%. The value of t is especially sensitive to the value of T, m_s, m_1, and m_0.

$$C = \frac{m_1+m_0-m}{m_{Fe}+m_1+m_0-m} \qquad \textbf{Eqn. 29}$$

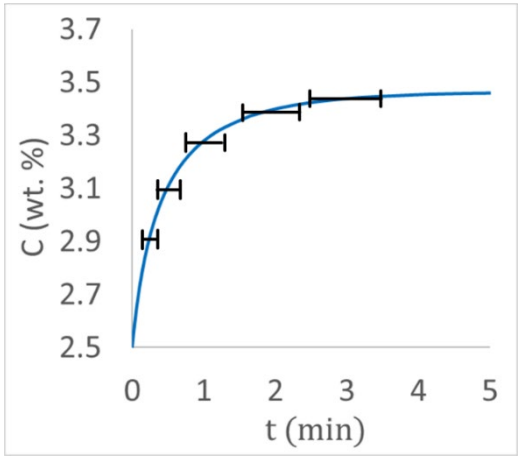

Figure 9. C(t) for Graphite 1 is calculated from m(t) using Eqn. 29 (T = 2696F (1480C), k = 10^{-4}m s^{-1}).

PRACTICAL IMPLICATIONS FOR RECARBURIZER ADDITIONS TO MOLTEN IRON

While the model described above is intended to be a step forward in the theoretical description of recarburizer dissolution, another important aim is to better understand (and quantify, where possible) the effects of key variables on carbon recovery. Here the model is used to illustrate quantitatively the effects of particle size, agitation, temperature, and the nature of the recarburizer on dissolution time. The influence of certain operational practices in the foundry is also addressed.

PARTICLE SIZE DISTRIBUTION

Since dissolution rate varies directly with the interfacial surface area (Eqns. 3 and 12), it is to be expected that the particle size distribution of the recarburizer will impact the dissolution time. Assume a spherical graphite particle with a typical density of 1500 kg m^{-3} with only its external surface being accessible to the iron. Equation 30 shows that the specific interfacial surface area (S_{sp}) varies inversely with the diameter (D). The corresponding plot in Figure 10 shows the rapid increase in S_{sp} as D decreases. The diameter range in Figure 10 covers the majority of commercial recarburizers. The mass fraction of particles with sizes below 0.2 mm (70 mesh) and above 9.5 mm (3/8” mesh) is normally limited in practice. The former tend to get entrained in air currents above the furnace, preventing their exposure to the iron. The latter have total dissolution times that are regarded as too long for most melt operations.

$$S_{sp} = \frac{S}{m} = \frac{S}{\rho V} = \frac{3}{\rho r} = \frac{6}{\rho D} \qquad \textbf{Eqn. 30}$$

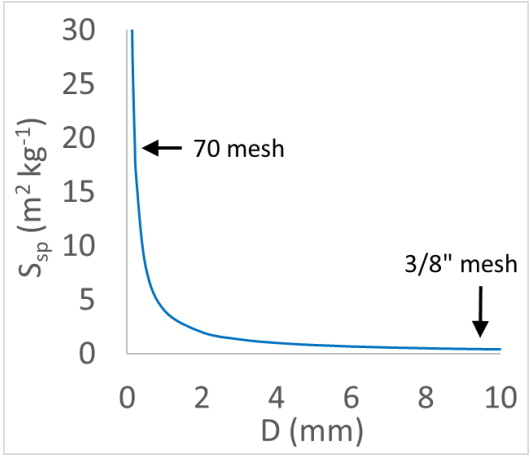

Figure 10. The specific interfacial surface area (S_{sp}) of a hypothetical synthetic graphite (ρ = 1500 kg m^{-3}) varies inversely with the diameter (D).

Table 8 shows the initial masses of the particle fractions and the total initial surface area for four simulated graphite recarburizers. The effect of the particle size distribution on the dissolution curve is evident in Figure 11. While all of the recarburizers effectively dissolve completely within five minutes, the 3/8" x 10M graphite takes nearly seven times as long as the 20M x 70M graphite to reach 90% recovery. Whether finer graphites can and should be used in practice, however, depends on their cost and availability as well as any tendency they may have to delay the wetting process by forming agglomerates (due to the smaller interstitial voids between particles).

It has been assumed to this point that only the external surface of the graphite particles is accessible to the iron. All recarburizers, however, exhibit a certain degree of porosity.[32, 33, 34] If pores are accessible to the iron during dissolution, the portion of the carbon that surrounds the pore is part of the interfacial surface area and should be included in the calculation of *S*. The extent to which the iron can penetrate the pore network of a carbon particle depends on the size of the pores and the viscosity of the iron, among other factors. The scanning electron micrographs of the carbon/iron interface published to date for recarburizers exposed to molten iron suggest that the penetration of the iron into the pore network is limited.[35, 36] Moreover, the dissolution curve in Figure 9 is generally consistent with the experimental data reported for graphite by other investigators (Table 7), which implies that the assumption of inaccessible pores is reasonable.[Error! Bookmark not defined.,Error! Bookmark not defined.,Error! Bookmark not defined.,Error! Bookmark not defined.,Error! Bookmark not defined.,Error! Bookmark not defined.,Error! Bookmark not defined.] The specific surface area for a typical recarburizer is another point worth considering. This is normally in the range of 1-3 $m^2\ g^{-1}$, regardless of the molecular structure of the recarburizer.[Error! Bookmark not defined.a, 37,38] In contrast, the initial interfacial surface area of Graphite 1 is 0.00352 $m^2\ g^{-1}$. As the dissolution rate varies directly with the interfacial surface area, complete access to the pores in the graphite would result in a dissolution rate two to three orders of magnitude greater. Such rapid dissolution is implausible, which suggests that the majority of the pores (and, perhaps, virtually all of them) are inaccessible until they eventually appear on the external surface during the dissolution process.

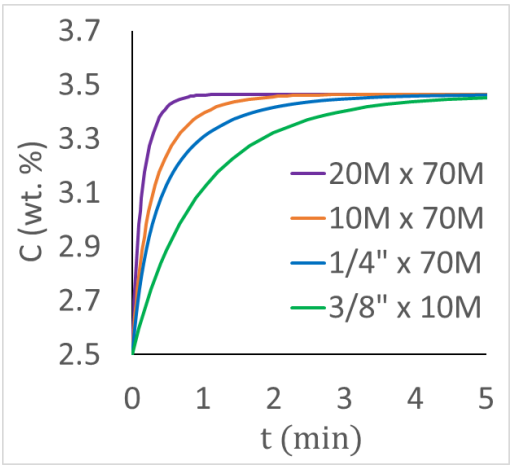

Figure 11. The higher specific surface area associated with a finer particle size distribution leads to faster dissolution for a hypothetical synthetic graphite (T = 2696F (1480C), k = 10^{-4} m s^{-1}, ρ = 1500 kg m^{-3}).

AGITATION OF THE IRON

The value of *k* accounts for the agitation of the iron as well as the temperature and the nature of the recarburizer. Figure 12 illustrates the effect of *k* on the dissolution curve for Graphite 1. As one would expect, lower *k*-values correspond to longer dissolution times. Not all of the curves are distinguishable, however, after accounting for a relative uncertainty of 20%. If the difference in *k* values is an order of magnitude (which is quite possible, in practice, if there is a large difference in agitation between production runs), the curves are clearly distinguishable. Indeed, a *k* value that is ten times lower implies that it takes ten times longer to reach any given point of carbon recovery, all other factors being equal.

Table 8. Simulated Initial Masses of the Weight Fractions and Total Initial Surface Area for Graphite Recarburizers

	Nominal Sizing			
	3/8" x 10M (9.5 x 2.0 mm)	**1/4" x 70M (6.4 x 0.21 mm)**	**10M x 70M (2.0 x 0.21 mm)**	**20M x 70M (0.85 x 0.21 mm)**
-3/8"/+1/4"	6.0	2.0	0.0	0.0
-1/4"/+6M	33.3	11.1	0.0	0.0
-6M/+10M	60.7	20.2	0.0	0.0
-10M/+20M	0.0	44.4	66.5	0.0
-20M/+40M	0.0	14.8	22.1	66.1

-40M/+50M	0.0	5.1	7.6	22.7
-50M/+70M	0.0	2.5	3.7	11.2
m_0 (kg)	100.0	100.0	100.0	100.0
S_0 (m^2)	121	352	468	840

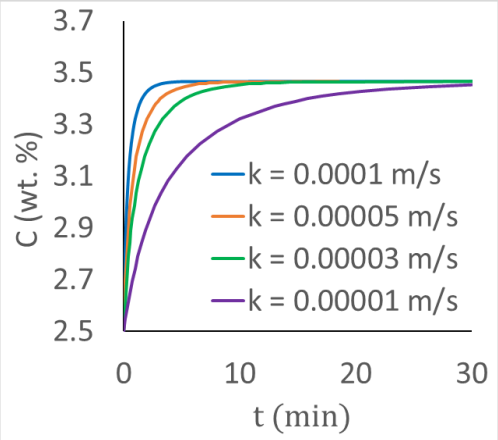

Figure 12. Greater agitation of the iron leads to higher values of the dissolution coefficient, k, and faster dissolution (T = 2696F (1480C)).

TEMPERATURE

The temperature dependence of $C(t)$ arises primarily from the temperature dependence of k. This effect is commonly predicted using the Arrhenius equation (Eqn. 31), where K is the apparent dissolution coefficient (s^{-1}; identical to K in Eqn. 5), A is a pre-exponential factor (s^{-1}; assumed to be temperature-independent for purposes of this analysis), E_a is the activation energy (kJ mol^{-1}), R is the universal gas constant (8.314 x 10^{-3} kJ mol^{-1} K^{-1}), and T is the melt temperature (K). Since $K = kS/V$ at any given time t, the ratio of any two dissolution coefficients, k_1 and k_2, is equal to the ratio of the respective apparent dissolution coefficients, K_1 and K_2, at $t = 0$ (when the respective surface area $S_1 = S_2 = S_0$) (Eqn. 32). Let T_1 and T_2 be any two temperatures of the iron melt. Combining Eqns. 31 and 32 yields Eqn. 33.

$$K = Ae^{-\frac{E_a}{RT}} \qquad \textbf{Eqn. 31}$$

$$\frac{K_2}{K_1} = \frac{\frac{k_2 S_0}{V}}{\frac{k_1 S_0}{V}} = \frac{k_2}{k_1} \quad (t = 0) \qquad \textbf{Eqn. 32}$$

$$k_2 = k_1 \frac{K_2}{K_1} = k_1 e^{\frac{E_a}{R}\left(\frac{1}{T_2} - \frac{1}{T_1}\right)} \quad (t = 0) \qquad \textbf{Eqn. 33}$$

The value of E_a for the dissolution of graphite in molten iron has been reported to be in the range of 19-80 kJ mol^{-1}.[Error! Bookmark not defined.,Error! Bookmark not defined.,Error! Bookmark not defined.,Error! Bookmark not defined.,Error! Bookmark not defined.] This is a relatively low value, which reflects the diffusion-controlled dissolution of graphite in iron (or, equivalently, the high rate of dissociation of graphite at the interface with the iron). Assuming E_a = 50 kJ mol^{-1}, k_1 = 1.00 x 10^{-4} m s^{-1}, and T_1 = 1753K (2696F, 1480C), k_2 can be calculated for any other temperature T_2. As shown in Figure 13, the variation of k with T for Graphite 1 is nearly linear over the temperature range of 2516-2876F (1380-1580C) and it is relatively insensitive to T. An increase or decrease of 100°C (180°F) results in only a 20% change in the value of k. This is a direct consequence of the low value of E_a. The low sensitivity of k to temperature for Graphite 1 is reflected in the dissolution curves in Figure 14. Indeed, the curves are indistinguishable, assuming a relative error of 20%. Not all recarburizers are associated with diffusion-controlled dissolution and low E_a values, however. The effect of temperature is revisited after considering the influence of the molecular structure of the recarburizer.

MOLECULAR STRUCTURE OF THE RECARBURIZER

While a detailed analysis of the relationship between the molecular structure of a recarburizer and its dissolution curve is beyond the scope of this work, data from select studies reported in the literature allow interesting comparisons via the dissolution model described above. Cham *et al.* compared the dissolution of high-purity synthetic graphite with that of metallurgical cokes.[Error! Bookmark not defined.] They found the initial K value of the synthetic graphite to be 1.686 x 10^{-2} s^{-1} at 2687F (1475C). Measuring K at different temperatures permitted the calculation of the E_a, which was found to be 54 kJ mol^{-1}. On the other hand, the K and E_a values for the metallurgical cokes were in the range of 1.18-3.50 x 10^{-3} s^{-1} at 2687F (1475C) (on average, about seven times lower than K for the graphite) and 313-479 kJ mol^{-1}, respectively. The difference in the dissolution behavior of the cokes was attributed to the nature of the ash and its effect on the interfacial surface area. In another study, Jang *et al.* calculated an E_a of 442 kJ mol^{-1} for a metallurgical coke.[Error! Bookmark not defined.] Assume an intermediate case, in which K for a hypothetical metcoke (Metcoke 1) is seven times lower than that of Graphite 1 and the E_a is 400 kJ mol^{-1}.

Given that the metcokes were approximately 10 wt. % ash, it is estimated that the initial surface area of Metcoke 1 is 10% less than that of Graphite 1. For Graphite 1 with $k_g = 10^{-4}$ m s^{-1}, $K_g = k_g S_g/V = 2.46 \times 10^{-2}$ s^{-1} at $t = 0$. Therefore, $K_m = K_g/7 = 3.52 \times 10^{-3}$ s^{-1} for Metcoke 1 at $t = 0$ and $k_m = K_m V/S_m = 1.59 \times 10^{-5}$ m s^{-1}. The dissolution curves for Graphite 1 and Metcoke 1 are shown in Figure 15, where the effect of the lower dissolution coefficient for Metcoke 1 is easily seen.

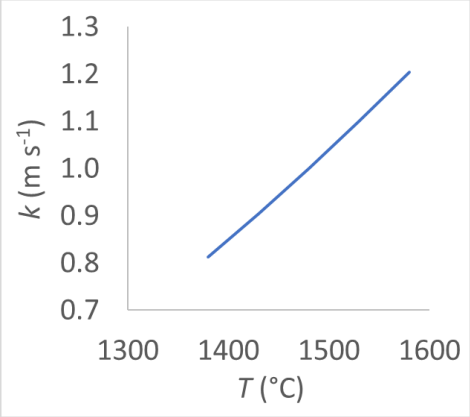

Figure 13. The temperature dependence of k for Graphite 1 in molten iron is nearly linear (E_a = 50 kJ mol^{-1}).

The effect of temperature on k is much more pronounced for Metcoke 1 than for Graphite 1 (Figure 16). Whereas the dependence of k on T is nearly linear for Graphite 1 (Figure 13), it is clearly exponential for Metcoke 1 over the same temperature range. This suggests that the dissociation of the carbon into individual atoms exerts a greater degree of control over the dissolution process for Metcoke 1 as compared to Graphite 1. Figure 17 shows the corresponding temperature effect on the dissolution curves for Metcoke 1. Taken together, Figures 14 and 17 demonstrate that the effect of temperature on dissolution rate becomes greater as k decreases. Whether the longer dissolution times typically observed in practice for less graphitic recarburizers are due to molecular structure, composition (e.g., ash and/or sulfur content), or both remains an open question.

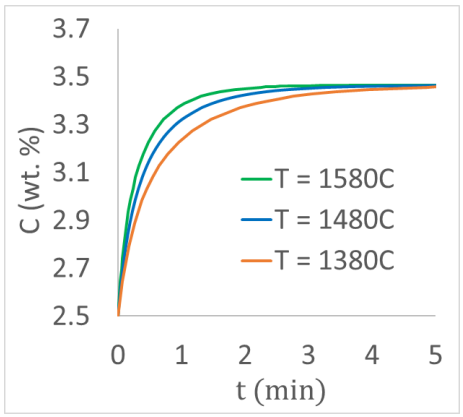

Figure 14. The effect of temperature on the dissolution rate for Graphite 1 is predicted to be relatively small, which is consistent with a diffusion-controlled dissolution process.

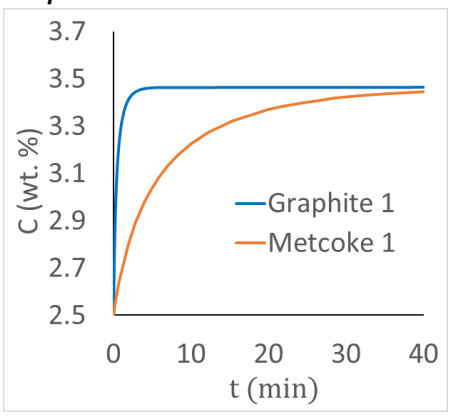

Figure 15. The nature and/or purity of the recarburizer has a substantial effect on the dissolution curve (T = 2696F (1480C)).

PRODUCTION PRACTICES IN THE FOUNDRY

The principles described above explain why certain production practices in the foundry can have a significant impact on recarburizer wetting and dissolution rates. Several of these practices were outlined by Linebarger.[39] It is important not to overfill the furnace, as the agitation of the iron at the top of the melt markedly decreases in such cases. Higher and faster carbon recoveries will result with little impact on iron throughput if proper melt levels are observed. Since the carbon dissolves faster as a result of increased agitation, the tap times can be reduced.

It is important to slag the furnace before a trim addition. This is to ensure that the carbon is immediately in direct contact with the iron instead of becoming coated with slag, which delays particle wetting. Moreover, energizing the furnace during a trim addition, if only for a couple minutes, has a substantial impact on the dissolution rate.

This is especially evident for diffusion-controlled dissolution, as is the case for graphite.

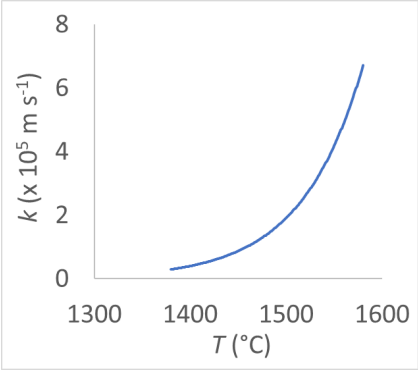

Figure 16. The temperature dependence of k for Metcoke 1 in molten iron is clearly exponential (E_a = 400 kJ mol^{-1}).

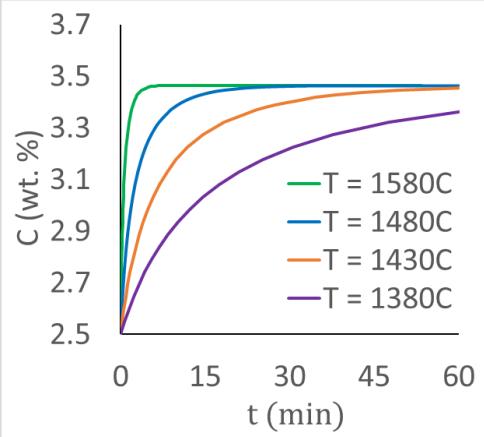

Figure 17. It is evident that the temperature has a substantial effect on the dissolution rate for Metcoke 1.

The dissolution curves in this work demonstrate that a small increase in the time allowed for the recarburizer to dissolve can have a large impact on carbon recovery. The model described herein allows a foundry to predict this carbon recovery as a function of time.

The order in which materials are charged to the furnace has an impact on recarburizer dissolution times. The best practice is to charge the recarburizer with the steel and before the pig iron. The reason is that the dissolution rate varies directly with the difference between the solubility of the recarburizer and its concentration at time t (Eqn. 3). This difference is greater for a recarburizer with a higher local concentration of steel, with its characteristic low carbon content.

CONCLUSION

The uniformly shrinking particle model can be incorporated into the classical diffusion layer model of dissolution to predict the dissolution curve for a recarburizer. Utilizing a transformation of the standard mass distribution of particle size to the corresponding number distribution and applying the shrinking particle model, the method explicitly accounts for the continually changing surface area of a polydisperse recarburizer as it dissolves. The model has been applied to a hypothetical graphite addition for a ductile iron, yielding a total dissolution time that is consistent with experimental data reported in the literature. The expected trends in dissolution time with changes to the particle size distribution, agitation of the iron, temperature, and nature of the recarburizer are observed. Moreover, the model is consistent with current best practices in foundry melt operations. The results indicate that the carbon/iron interface is largely limited to the external surface of the particle, a reasonable finding in light of SEM images that have been published by investigators.

The key limitation of the model in its current form is the assumption that the entire external surface of the recarburizer is wetted at t = 0. A more robust model would incorporate the time lag between the addition of the recarburizer and the time at which its entire accessible surface is wetted. Accounting for particles of irregular shape, any penetration of the iron into the pores of the recarburizer particles, any particle breakup, oxidation of the carbon during the dissolution process, and the time required for heat transfer from the iron to the carbon would also be expected to improve the accuracy of the model.

ACKNOWLEDGMENTS

The author would like to acknowledge Ken Way, whose helpful suggestions enhanced the quality of this work.

APPENDIX: ANALYTICAL SOLUTION TO THE HIXSON-CROWELL EQUATION

Here the derivation of Eqn. 28 is provided. The solution was initially generated using the online tool Integral Calculator.[40] That tool provided the analytical solution to the integral on the left-hand side of Eqn. 27 as well as a high-level summary of the steps involved. However, a complete derivation is required to prove that Eqn. 28 is correct. The derivation begins with Eqn. 27, the Hixson-Crowell expression for Graphite 1:

$$\int \frac{1}{(am^2+bm)(m_s-m_1-m_0+m)}dm = \int -\frac{k}{V}dt \qquad \textbf{Eqn. 27}$$

Factoring the denominator on the left-hand side (LHS) of Eqn. 27 gives

$$\text{LHS} = \int \frac{1}{m(am+b)(m_s-m_1-m_0+m)}dm \qquad \textbf{Eqn. 34}$$

Partial fraction decomposition leads to

$$\text{LHS} = \int \left(\frac{A}{m} + \frac{B}{am+b} + \frac{C}{m_s-m_1-m_0+m}\right)dm \qquad \textbf{Eqn. 35}$$

Combining Eqns. 34 and 35 yields

$$A(am+b)(m_s-m_1-m_0+m) + Bm(m_s-m_1-m_0+m) + Cm(am+b) = 1 \qquad \textbf{Eqn. 36}$$

Because Eqn. 36 is true for all m, it can be solved for A, B, and C by substituting convenient values for m.[41] f $m = 0$, then

$$A = \frac{1}{b(m_s-m_1-m_0)} \qquad \textbf{Eqn. 37}$$

If $m = -b/a$, then

$$B\left(-\frac{b}{a}\right)\left(m_s-m_1-m_0-\frac{b}{a}\right) = 1 \qquad \textbf{Eqn. 38}$$

This can be written

$$B = \frac{a^2}{-ab\left(m_s-m_1-m_0-\frac{b}{a}\right)} \qquad \textbf{Eqn. 39}$$

and, therefore,

$$B = \frac{a^2}{b[a(m_1+m_0-m_s)+b]} \qquad \textbf{Eqn. 40}$$

Letting $m = m_1 + m_0 - m_s$ yields

$$C = \frac{1}{(m_1+m_0-m_s)[a(m_1+m_0-m_s)+b]} \qquad \textbf{Eqn. 41}$$

Combining Eqns. 36, 37, 40, and 41 gives

$$\text{LHS} = \int \left(\frac{1}{b(m_s-m_1-m_0)m} + \frac{a^2}{b[a(m_1+m_0-m_s)+b](am+b)} + \frac{1}{(m_1+m_0-m_s)[a(m_1+m_0-m_s)+b](m_s-m_1-m_0+m)}\right)dm \qquad \textbf{Eqn. 42}$$

Therefore,

$$\text{LHS} = \frac{1}{b(m_s - m_1 - m_0)} \int \frac{1}{m} dm + \frac{a^2}{b[a(m_1 + m_0 - m_s) + b]} \int \frac{1}{am + b} dm + \frac{1}{(m_1 + m_0 - m_s)[a(m_1 + m_0 - m_s) + b]} \int \frac{1}{m_s - m_1 - m_0 + m} dm \quad \textbf{Eqn. 43}$$

Solving the first integral in Eqn. 43 yields

$$\int \frac{1}{m} dm = \ln|m| + D \quad \textbf{Eqn. 44}$$

The second integral is solved by letting $u = am + b$. Thus, $dm = du/a$ and

$$\int \frac{1}{am + b} dm = \int \frac{1}{u} \frac{1}{a} du = \frac{1}{a} \ln|am + b| + E \quad \textbf{Eqn. 45}$$

Finally, the third integral is solved by letting $u = m_s - m_1 - m_0$. Then $du = dm$ and

$$\int \frac{1}{m_s - m_1 - m_0 + m} dm = \int \frac{1}{u} du = \ln|m_s - m_1 - m_0 + m| + F \quad \textbf{Eqn. 46}$$

Since the arguments of the logarithmic functions in Eqns. 44, 45, and 46 (m, $am + b$, and $m_s - m_1 - m_0 + m$, respectively) have only positive values in practice, the absolute value symbols in Eqns. 44-46 can be omitted. The combination of Eqns. 43-46 leads to

$$\text{LHS} = \frac{\ln m}{b(m_s - m_1 - m_0)} + \frac{a \ln(am + b)}{b[a(m_1 + m_0 - m_s) + b]} + \frac{\ln(m_s - m_1 - m_0 + m)}{(m_1 + m_0 - m_s)[a(m_1 + m_0 - m_s) + b]} + G \quad \textbf{Eqn. 47}$$

where $G = D + E + F$ is the combined constant of integration. The expression can be simplified using the lowest common denominator:

$$\text{LHS} = \frac{a(m_1 + m_0 - m_s) \ln(am + b) + b \ln(m_s - m_1 - m_0 + m) - [a(m_1 + m_0 - m_s) + b] \ln m}{b(m_1 + m_0 - m_s)[a(m_1 + m_0 - m_s) + b]} + G \quad \textbf{Eqn. 48}$$

Integrating the right-hand side of Eqn. 27 and combining Eqns. 27 and 48 yields

$$\frac{a(m_1 + m_0 - m_s) \ln(am + b) + b \ln(m_s - m_1 - m_0 + m) - [a(m_1 + m_0 - m_s) + b] \ln m}{b(m_1 + m_0 - m_s)[a(m_1 + m_0 - m_s) + b]} = -\frac{k}{V} t + G \quad \textbf{Eqn. 49}$$

Since $m = m_0$ at $t = 0$, the initial value of the LHS of Eqn. 49 is

$$G = \frac{a(m_1 + m_0 - m_s) \ln(am_0 + b) + b \ln(m_s - m_1) - [a(m_1 + m_0 - m_s) + b] \ln m_0}{b(m_1 + m_0 - m_s)[a(m_1 + m_0 - m_s) + b]} \quad \textbf{Eqn. 50}$$

Finally, substituting $h = m_1 + m_0 - m_s$ (for simplicity) and combining Eqns. 49 and 50 produces the final solution (which is identical to Eqn. 28).

$$\frac{ah \ln(am_0 + b) + b \ln(m_s - m_1) - (ah + b) \ln m_0}{bh(ah + b)} - \frac{ah \ln(am + b) + b \ln(m - h) - (ah + b) \ln m}{bh(ah + b)} = \frac{k}{V} t \quad \textbf{Eqn. 51}$$

REFERENCES

1. Fick, A., "Ueber Diffusion," *Annalen der Physik* 170, 59-86 (1855). https://doi.org/10.1002/andp.18551700105 (Link last accessed 03-10-2025.).
2. Noyes, A.A., Whitney, W.R., "The Rate of Solution of Solid Substances in Their Own Solutions," *J. Am. Chem. Soc.* 19, 930-934 (1897). https://doi.org/10.1021/ja02086a003 (Link last accessed 03-10-2025.).
3. Siepmann, J., Siepmann, F., "Mathematical Modeling of Drug Dissolution," *Int. J. Pharm.* 453, 12-24 (2013). https://doi.org/10.1016/j.ijpharm.2013.04.044 (Link last accessed 03-10-2025.).
4. Dahlke, V.O., Knacke, O. "Die Auflösung von Kohlenstoff in flüssigem Eisen," *Archiv für das Eisenhüttenwesen* 26, 373-378 (1955). https://doi.org/10.1002/srin.195502054 (Link last accessed 03-10-2025.).
5. Bandyopadhyay, D., Singh, S.D., Sanyal, D., Singh, K.K., Singh, K.N., "A Study on Dissolution Kinetics of Carbon in Liquid Iron Bath," *Chem. Eng. J.* 94, 79-92 (2003). https://doi.org/10.1016/S1385-8947(02)00030-X (Link last accessed 03-10-2025.).
6. Cham, S.T., Sahajwalla, V., Sakurovs, R., Sun, H., Dubikova, M. "Factors Influencing Carbon Dissolution from Cokes into Liquid Iron," *ISIJ Int.* 44, 1835-1841 (2004). https://doi.org/10.2355/isijinternational.44.1835 (Link last accessed 03-10-2025.).
7. Cham, S.T., Sakurovs, R., Sun, H., Sahajwalla, V., "Influence of Temperature on Carbon Dissolution of Cokes in Molten Iron," *ISIJ Int.* 46, 652-659 (2006). https://doi.org/10.2355/isijinternational.46.652 (Link last accessed 03-10-2025.).
8. Cham, S.T., "Investigating Factors that Influence Carbon Dissolution from Coke into Molten Iron," Doctoral Dissertation, University of New South Wales, Sydney, Australia (2007). https://doi.org/10.26190/unsworks/17751 (Link last accessed 03-10-2025.).
9. Chapman, M., Monaghan, B.J., Nightingale, S., Mathieson, J., Nightingale, R. "Formation of a Mineral Layer During Coke Dissolution into Liquid Iron and Its Influence on the Kinetics of Coke Dissolution Rate," *Metall. Mater. Trans. B* 39, 418-430 (2008). https://doi.org/10.1007/s11663-008-9145-7 (Link last accessed 03-10-2025.).
10. Chapman, M.W., Monaghan, B.J., Nightingale, S.A., Mathieson, J.G., Nightingale, R.J., "The Effect of Sulfur Concentration in Liquid Iron on Mineral Layer Formation During Coke Dissolution," *Metall. Mater. Trans. B* 42, 642-651 (2011). https://doi.org/10.1007/s11663-011-9519-0 (Link last accessed 03-10-2025.).
11. Deng, Y., Zhang, J.-l., Jiao, K.-x., "Dissolution Mechanism of Carbon Brick into Molten Iron," *ISIJ Int.* 58, 815-822 (2018). https://doi.org/10.2355/isijinternational.ISIJINT-2017-659 (Link last accessed 03-10-2025.).
12. Jang, D., Kim, Y., Shin, M., Lee, J., "Kinetics of Carbon Dissolution of Coke in Molten Iron," *Metall. Mater. Trans. B* 43, 1308-1314 (2012). https://doi.org/10.1007/s11663-012-9724-5 (Link last accessed 03-10-2025.).
13. Kosaka, M., Minowa, S., "On the Rate of Dissolution of Carbon into Molten Fe-C Alloy," *Trans. ISIJ* 8, 392-400 (1968). https://doi.org/10.2355/isijinternational1966.8.392 (Link last accessed 03-10-2025.).
14. Shigeno, Y., Tokuda, M., Ohtani, M. "The Dissolution Rate of Graphite into Fe–C Melt Containing Sulphur or Phosphorus," *Trans. Jpn. Inst. Met.* 26, 33-43 (1985). https://doi.org/10.2320/matertrans1960.26.33 (Link last accessed 03-10-2025.).
15. Sun, H. "Analysis of Reaction Rate Between Solid Carbon and Molten Iron by Mathematical Models," *ISIJ Int.* 45, 1482-1488 (2005). https://doi.org/10.2355/isijinternational.45.1482 (Link last accessed 03-10-2025.).
16. Sun, H., Mori, K., Sahajwalla, V., Pehlke, R. D., "Carbon Solution in Liquid Iron and Iron Alloys," *High Temp. Mater. Process.* 17, 257-270 (1998). https://doi.org/10.1515/HTMP.1998.17.4.257 (Link last accessed 03-10-2025.).
17. Sun, M., Pang, K., Zhang, J., Li, K., Li, H. "In Situ Monitoring and Dissolution Limit of Carbon Dissolution in Hot Metal," *Steel Res. Int.* 92 (2021). https://doi.org/10.1002/srin.202100111 (Link last accessed 03-10-2025.).
18. Wright, J.K., Denholm, W.T., "Dissolution of Particulate Carbon in a Turbulent Iron Bath," *Australasian Inst. Mining Metall., Symposium on Extractive Metallurgy* 323–29 (1984).
19. Wright, J.K., Taylor, I.F., "Multiparticle Dissolution Kinetics of Carbon in Iron-Carbon-Sulphur Melts," *ISIJ Int.* 33, 529-538 (1993). https://doi.org/10.2355/isijinternational.33.529 (Link last accessed 03-10-2025.).
20. Hsu, J.-P., Liu, B.-T. "Dissolution of Solid Particles in Liquids: A Reaction-Diffusion Model," *Colloids Surf.* 69, 229-238 (1993). https://doi.org/10.1016/0166-6622(93)80004-Y (Link last accessed 03-10-2025.).
21. Jiang and coworkers have found via molecular dynamics simulation that the dissociation of carbon in molten iron may consist of diatomic or triatomic carbon chains as well as single carbon atoms. See Jiang, C., Zhang, J., Li, K., Liang, W., Zhisheng, B. "Influence of Graphite Crystalline Orientation on the Carbon Dissolution Reaction in Liquid Iron: A ReaxFF Molecular Dynamics Simulation Study," *J. Mol. Liq.* 335, 115688-115695 (2021). https://doi.org/10.1016/j.molliq.2021.115688 (Link last accessed 10-26-2024).
22. Hixson, A.W., Crowell, J.H. "Dependence of Reaction Velocity upon Surface and Agitation," *Ind. Eng. Chem.* 23, 923-931 (1931). https://doi.org/10.1021/ie50260a018 (Link last accessed 03-10-2025.).

23. The representation of each particle mass fraction by the midpoint of the radius range for that fraction is less than ideal. However, the loss of accuracy is not necessarily large. An attempt to improve the resolution of the model by fitting curves to portions of the particle distribution and using interpolation to generate additional particle fractions resulted in a change in the corresponding total surface area of about 5%.
24. In practice, the number of particle size categories used to report the mass distribution for a recarburizer is often relatively small. Moreover, the distribution is not always easily modeled as a continuous function. The quantitative treatment here employs a discrete particle size distribution for these reasons. However, this choice is entirely optional, and the summations in this treatment may be replaced by integrals, as appropriate. It should be noted that the conversion of a continuous mass distribution to a continuous number distribution (required to calculate surface area) is not necessarily trivial. For a recent quantitative analysis of this problem, see: Camalan, M., "Estimating the Number-Weighted Equivalents of the Mass-Weighted Size Distribution Functions," *Powder Technol.* 369, 106-113 (2020). https://doi.org/10.1016/j.powtec.2020.05.011 (Link last accessed 03-10-2025.).
25. Bullard, J.W.; Jin, Q.; Snyder, K.A. "How Do Specific Surface Area and Particle Size Distribution Change When Granular Media Dissolve?" *Chem. Eng. J.* 406, 127098 (2021). https://doi.org/10.1016/j.cej.2020.127098 (Link last accessed 03-10-2025.).
26. Assuming that the agitation in the vicinity of a particle is independent of particle size, the dissolution flux should also be independent. Wright and Taylor have shown that the diffusion coefficient is approximately independent of particle size for particles with diameters greater than 0.1 mm,[Error! Bookmark not defined.] which is the case for most recarburizers.
27. Metzloff, K.E., Nelson, R.D., Loper, C.R., Jr. "Carbon Dissolution in Cast Iron Melts Reexamined," *Trans. AFS* Paper 05-168 (2005).
28. The data was fit with $S = am^2 + bm$ instead of the more common $S = am^2 + bm + c$ to avoid complications with the subsequent integration. Given that $c \approx 0$ for the best fit of the data, the effect on the final solution is negligible.
29. Equation 20 gives an indeterminate result for $m = 0$.
30. Loper, C.R., Jr., Liu, S.L., Shirvani, S., Witter, T.H. "The Dissolution of Carbon in Cast Iron Melts as Studied Using Commercial Carbon Raisers and Experimental Materials," *Trans. AFS* 92, 323-335 (1984).
31. Holm, K. "The Properties of Calcined Anthracite," *Master Thesis* (2017).
32. Ellis, P.J., Bacha, J.D. "Shot Coke," *Light Metals 1996, The Minerals, Metals, and Materials Society* 477-484 (1996).
33. Paul, R.J. "Application of a Three-Dimensional Random Pore Model for Thermal Oxidation of Synthetic Graphite," *J. Nucl. Mater.* 543, 152589 (2021). https://doi.org/10.1016/j.jnucmat.2020.152589 (Link last accessed 03-10-2025.).
34. Sun, M.-M., Zhang, J.-L., Li, K.-J., Li, H.-T., Wang, Z.-M., Jiang, C.-H., Ren, S., Wang, L., Zhang, H. "The Interfacial Behavior Between Coke and Liquid Iron: A Comparative Study on the Influence of Coke Pore, Carbon Structure and Ash," *J. Mater.* 72, 2174-2183 (2020). https://doi.org/10.1007/s11837-020-04048-0 (Link last accessed 03-10-2025.).
35. Zhu, H.-b., Zhan, W.-l,, Yu, Y.-c., He, Z.-j., Pang, Q.-h., Zhang, J.-h. "Wetting and Spreading Behavior of Molten Iron in Contact with Graphite Substrate: Interfacial Effects," *Fuel Process. Technol.* 203, 106389 (2020). https://doi.org/10.1016/j.fuproc.2020.106389 (Link last accessed 03-10-2025.).
36. Subero, J. "Quality of Calcined Petroleum Coke and Its Influence on Aluminum Smelting," *Light Metals 2013, The Minerals, Metals and Materials Series* 1085-1088 (2013). https://doi.org/10.1007/978-3-319-65136-1_183 (Link last accessed 03-10-2025.).
37. Baklanova, O.N., Drozdov, V.A., Lavrenov, A.V., Vasilevich, A.V., Muromtsev, I.V., Trenikhin, M.V., Arbuzov, A.B., Likholobov, V.A., Gorbunova, O.V. "Mechanical Activation of Graphite in Air: A Way to Advanced Carbon Nanomaterials," *J. Alloys Compd.* 646, 145-154 (2015). https://doi.org/10.1016/j.jallcom.2015.05.090 (Link last accessed 03-10-2025.).
38. Linebarger, F. "It Doesn't Melt, It Dissolves," *Techtalk* 29, Miller and Company (2005).
39. https://www.integral-calculator.com/# (Link last accessed 03-10-2025.).
40. Larson, R., Edwards, B. "Calculus," Cengage, Boston, MA (2023).